Adaptive Variable Angle Control in Switched Reluctance Motor Drives for Electric Vehicle Applications

He Cheng[†], Hao Chen[*], Shaohui Xu[*], and Shunyao Yang[*]

[†,*]School of Electrical and Power Engineering, China University of Mining and Technology, Xuzhou, China

Abstract

Switched reluctance motor (SRM) is suitable for electric vehicle (EV) applications with the advantages of simple structure, good overload capability, and inherent fault-tolerance performance. The SRM dynamic simulation model is built based on torque, voltage, and flux linkage equations. The EV model is built on the basis of the analysis of forces acting on a vehicle. The entire speed range of the SRM drive is then divided into constant torque and constant power areas. The command torque of the motor drive system is given according to the accelerator pedal coefficient and motor operation areas. A novel adaptive variable angle control is proposed to avoid the switching chattering between the current chopping control and angle position control modes in SRM drives for EV applications. Finally, simulation analysis and experimental results are conducted to verify the accuracy of the proposed simulation model and control strategy.

Key words: Adaptive variable angle control, Constant power area, Constant torque area, Electric vehicle, Switched reluctance motor

I. INTRODUCTION

The development of the automobile industry aggravates environment pollution and energy crisis. Electric vehicles (EVs) have received increasing attention worldwide because of low noise, high efficiency, and less pollution emission [1]-[3]. Switched reluctance motor (SRM) has several advantages, such as a simple structure, four-quadrant operation, wide extended speed range, robustness, and the potential to operate at high rotational speeds. These features make SRM an attractive solution for the drivetrains of EV applications [4]-[7].

In [8], a comparison of the energy consumption of the interior permanent magnet synchronous motors (IPMSMs) and SRMs in four driving schedules was conducted. The results showed that SRM has higher efficiency than IPMSM in high speed range. Thus, the SRM has better performance in Highway Fuel Economy Driving Schedule and in New European Driving Cycle. In addition, SRMs exhibit superiority if EVs are equipped with high gear ratio. An SRM with a high number of rotor poles was comprehensively evaluated for traction application in EVs in [9]. These types of SRM have better self-starting and fault tolerance capabilities than the conventional SRM. An SRM with segmented rotor construction for direct drive application was proposed in [10]. The drive efficiency and power density of the SRM could be enhanced because of low iron weight and short flux paths. In [11], the design indicators and design procedure of SRM for EVs were proposed. Based on these indicators, multi-objective optimization method was adopted to obtain the stator winding turns, pole arc width, and air gap length. A detailed model of SRM drive and power converter, which covers motoring and generating modes of EV, was developed in [12]. A multi-objective power flow control method with repetitive controller was proposed to restrain battery current ripple based on the above model. In [13], a finite horizon linear quadratic regulator was proposed for the current control of an SRM. This method could cope with the measurement noise and uncertainties within the machine inductance profile. A novel phase current reconstruction method from the dc-link current employing double

high-frequency pulse injection was proposed in [14]; this method uses only one current sensor in the dc link and requires no additional circuits. An offline torque-sharing function (TSF) for torque ripple reduction in SRM drive was proposed in [15]. The maximum ripple-free torque speed of the selected offline TSF was seven times as high as the best case in conventional TSFs. In [16], a direct instantaneous torque control (DITC) with wide operating range for SRMs was presented. Compared with the conventional DITC, the proposed DITC could reduce the torque ripple without the additional optimization strategy for switching angles.

Different control techniques have been proposed to improve the operation performance of SRM drives. However, few of them consider the systematic design and control in SRM drives for EV applications. In the present study, an optimal three-phase 12/8 pole SRM is adopted for EV drive motor [17]. The dynamic simulation model is built to analyze the motor mechanical characteristic, and the torque commands are given according to the accelerator pedal coefficient in the constant torque and constant power areas to exploit the torque output capability of the SRM. A novel adaptive variable angle control (AVAC) is proposed to implement a seamless transition between the current chopping control (CCC) and angle position control (APC) without considering load variations. The EV simulation model is built based on vehicle dynamic equations to demonstrate the proposed control strategy. Finally, experimental results are presented to validate the feasibility and accuracy of the proposed control method on a small EV prototype.
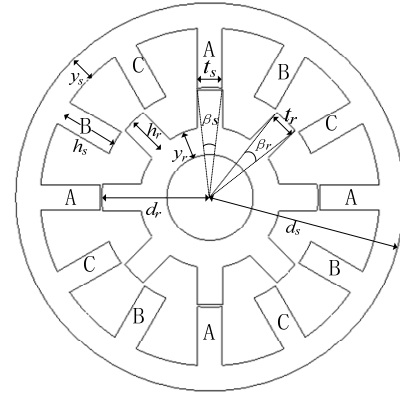
II. DYNAMIC SIMULATION MODEL OF SRM

An optimal three-phase 12/8 pole SRM is designed for EV drive motor [11]. Fig. 1(a) shows the cross-sectional profile of the SRM. Figs. 1(b), 1(c), and 1(d) show the torque/power–speed characteristics, flux linkage–current–position characteristics, and torque–position–current characteristics, respectively. The SRM parameters are listed in Table I.

Fig. 1(c) shows that the SRM usually works in saturation state. The flux linkage, inductance, and torque are highly coupled and nonlinear with the variation of rotor position and phase current. Hence, magnetization characteristics are difficult to decouple and model mathematically. The induced electromagnetic torque for a specified current can be obtained by differentiating the coenergy $W_m{}'$ with respect to the rotor position θ, which can be expressed as
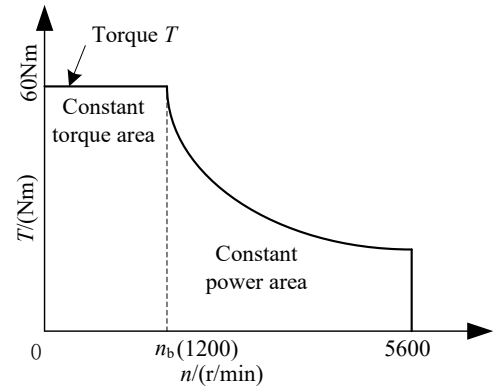
$$T_e = \frac{\partial W_m{}'}{\partial \theta}\Big|_{i=const}, \tag{1}$$

where $W_m{}'$ stands for coenergy, T_e represents electromagnetic torque, and i denotes phase current.
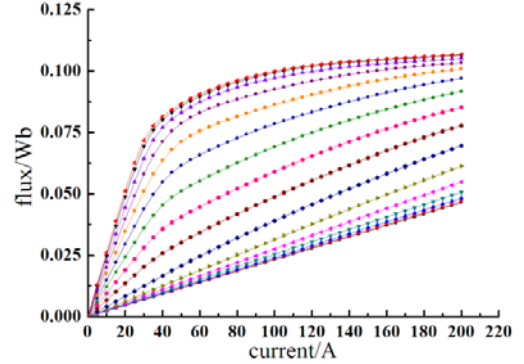
The obtained coenergy is equal to the area enclosed by the λ–i curve over one excitation cycle and can be expressed as
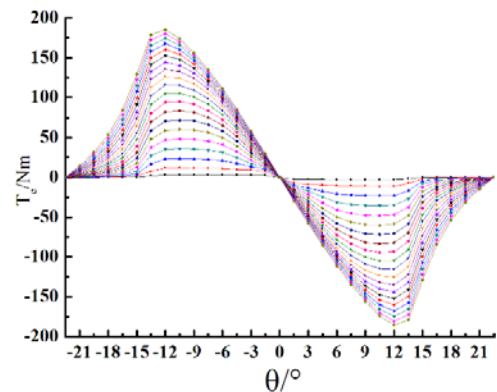

(a) Cross-sectional profile of SRM.

(b) Torque/power–speed characteristics.

(c) Flux linkage–current–position characteristics.

(d) Torque–position–current characteristics.

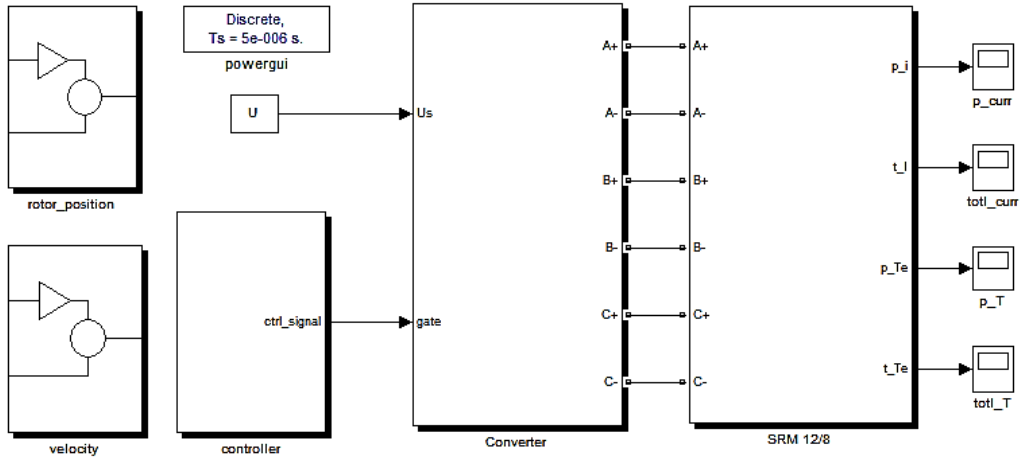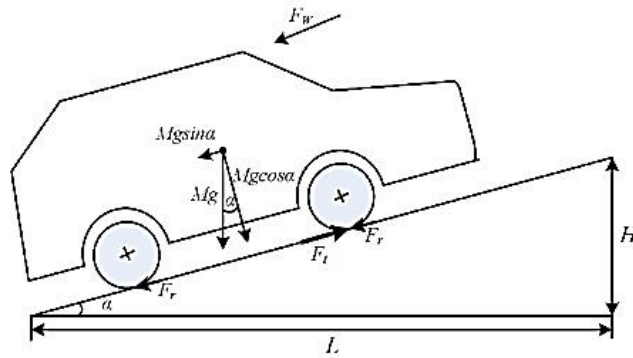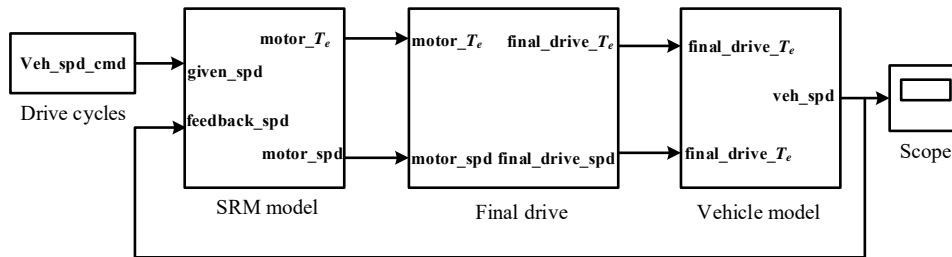Fig. 1. Optimal three-phase 12/8 pole SRM.

Fig. 2. SRM dynamic simulation model.

(a) Force analysis of EV on the slope.

(b) EV simulation model.

Fig. 3. EV model.

$$W_m' = \int_0^i \psi \, di \,, \tag{2}$$

where ψ denotes winding flux linkage.

The phase voltage equation is

$$\psi = \int (u - Ri) \, dt + \psi_0 \,, \tag{3}$$

where R represents winding resistance, and u denotes winding voltage.

By combining the torque (1), coenergy (2), and flux linkage (3), the dynamic simulation model of the SRM drive is built based on the flux linkage–current position characteristics and torque–position–current characteristics, as shown in Fig. 2. The entire model consists of the rotor position and velocity calculation modules, and controller,

power converter, and SRM modules.

III. EV SIMULATION MODEL

Fig. 3(a) shows the force analysis of the EV on a slope. The forces include traction force F_t, aerodynamic resistance F_W, rolling resistance F_r, grading resistance F_g, and accelerating resistance F_a.

The traction force F_t is derived from the electromagnetic torque generated by the SRM, transferred through transmission, and finally driven to the drive wheels of the EV, which is expressed as

$$F_t = i_o \eta \frac{T_e}{R_w} \,, \tag{4}$$

TABLE I
SRM PARAMETERS

Parameters	Symbol	Value
Stator/Rotor	N_s/N_r	12/8
Stator radius (mm)	d_s	90
Rotor radius (mm)	d_r	49.5
Stator yoke thickness (mm)	y_s	11.5
Rotor yoke thickness (mm)	y_r	12.5
Stator pole length (mm)	h_s	28.5
Rotor pole length (mm)	h_r	17
Stator pole arc (°)	β_s	15
Rotor pole arc (°)	β_r	16
Iron length (mm)	L	150
Turns per pole	N	12
Air gap length (mm)	g	0.5

TABLE II
SIMULATION PARAMETERS OF EV

Parameters	Symbol	Value
Vehicle mass (kg)	M	800
Rolling resistance coefficient	f_r	0.01
Aerodynamic drag coefficient	C_D	0.23
Front area (m²)	A_f	2.0
Gravity acceleration (m/s²)	g	9.8
Air mass density (kg/m³)	ρ	1.205
Wheel diameter (m)	D_w	0.5
Final ratio	i_o	10
Rotational inertia factor	δ	1.05

where T_e is the motor electromagnetic torque, i_o is the gear ratio of the final drive, η is the efficiency of the driveline from the motor to the driven wheels, and R_w is the wheel radius.

The rolling resistance F_r caused by the friction of tires with the ground can be defined as

$$F_r = f_r Mg \cos\alpha, \qquad (5)$$

where f_r is the friction coefficient of rolling.

The aerodynamic resistance F_W is the wind resistive force opposing the EV movement, which is described as

$$F_W = \frac{1}{2}\rho A_f C_D V^2, \qquad (6)$$

where ρ is the air density, A_f is the frontal area of EV, and C_D is the aerodynamic drag coefficient.

The grading resistance F_g is the weight component of the EV that is always directed in the downward direction and can be expressed as

$$F_g = Mg \sin\alpha. \qquad (7)$$

The accelerating resistance F_a, which accelerates the EV can be described as

$$F_a = \delta M \frac{dV}{dt}, \qquad (8)$$

where δ is the mass factor that equivalently converts the

rotational inertias of rotating components into translational mass.

According to Newton's second law,

$$F_t = F_r + F_W + F_g + F_a. \qquad (9)$$

The vehicle model can be built based on vehicle dynamics ((4)–(9)). By combining the SRM model built in Part II, the entire EV simulation model is built in Matlab/Simulink, as shown in Fig. 3(b). It is composed of modules of drive cycle, SRM model, final drive, and vehicle model. The EV parameters are listed in Table II.

IV. CONTROL STRATEGIES OF SRM DRIVE FOR EV

To implement the smooth and dynamic acceleration process of the EV, the accelerator pedal coefficient $\gamma(k)$ is defined as

$$\gamma(k) = \begin{cases} 1 & v(k) \geq v_{\max} \\ \dfrac{v(k) - v_{\min}}{v_{\max} - v_{\min}} & v_{\min} \leq v(k) \leq v_{\max}, \\ 0 & v(k) < v_{\min} \end{cases} \qquad (10)$$

where $v(k)$ is the sampling value of the accelerator pedal; and $v_{\min}$ and $v_{\max}$ are the minimum and maximum sampling threshold values of the accelerator pedal.

As shown in Fig. 1(b), the base speed n_b divides the entire SRM speed range into constant torque and constant power areas. To exploit the torque output capability of the SRM, the relationships of motor command torque T_{ref} with accelerator pedal coefficient $\gamma(k)$ and motor speed n are set as follows:

$$T_{ref} = \begin{cases} \gamma(k)T_{\max} & n \leq n_b \\ \gamma(k)\dfrac{9.55P_{\max}}{n} & n > n_b \end{cases}, \qquad (11)$$

where $T_{\max}$ is the maximum torque in the constant torque area, and $P_{\max}$ is the maximum output power in the constant power area.

The SRM control structural diagram is proposed, as shown in Fig. 4. It is composed of torque controller, current controller, adaptive angle controller, logic synthesis unit, and torque estimator. The logic synthesis unit synthesizes the outputs of the current and adaptive angle controllers and inputs them into the asymmetrical half-bridge power converter. The accelerator pedal sampling signal $v(k)$ is converted into accelerator pedal coefficient $\gamma(k)$ according to (10). $\gamma(k)$ is then converted into motor reference torque T_{ref} according to (11). The reference torque T_{ref} and estimated torque T_e are inputted into the torque controller, which converts the torque error into three-phase current command i_{ref}. i_{ref} and the actual phase current i sensed by the Hall effect sensor are inputted into the hysteresis current controller. The chopping gating signals of insulated gate bipolar transistors (IGBTs) in an asymmetric half-bridge power inverter are generated by the logic synthesis unit. The average torque can
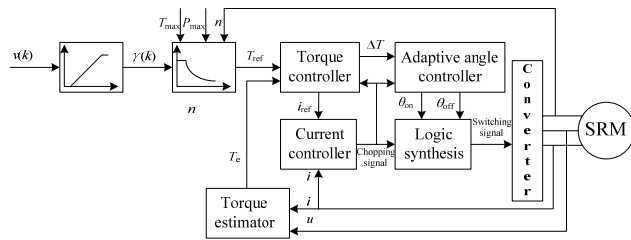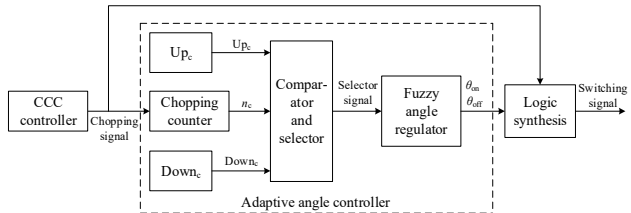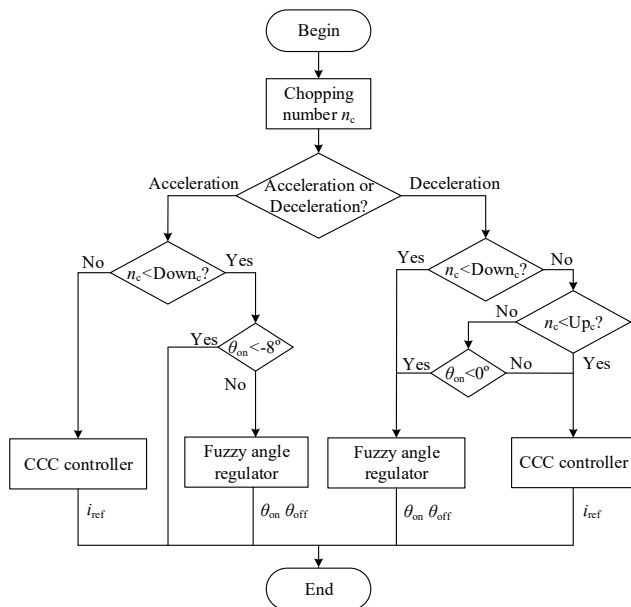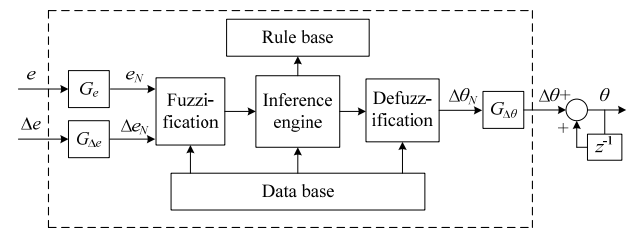
Fig. 4. SRM control structural diagram.

(a) Adaptive angle controller.

(b) Control flowchart and control rules.

(c) Fuzzy angle regulator.

Fig. 5. Structural diagram of adaptive variable angel control.

be estimated by the torque estimator based on (1), (2), and (3) [18].

Current controller is one of the most important parts of the SRM drive. Some current controllers have been investigated in [19]-[21], including gain-scheduling PI controller, predictive current controller, and sliding mode current

controller. Hysteresis current controller is one of the most well-known current controllers because of its simple structure, strong robustness, and fast dynamic response. The soft chopping mode is implemented in this study by using a digital controller to further reduce control complexity and switching frequency [22].

For SRM drives, CCC is usually adopted at low speed to limit the current amplitude, and APC is used to enhance the power output capability at high speed. If the load is constant, the speed, θ_{on} and θ_{off}, at the switching instants of the two modes can be determined by trial and error. However, for vehicle applications, the load changes with the road conditions and passenger numbers, and determining θ_{on} and θ_{off} is difficult at the instance of transition between CCC and APC. Improper switching angles will cause switching chattering and result in an unstable drive system. AVAC is proposed in this study to solve the aforementioned problems.

The structural diagram of AVAC is shown in Fig. 5(a), which is composed of CCC controller, chopping counter, comparator, selector, fuzzy angle regulator, upper-limit constant Up_c, and lower-limit constant $Down_c$. The control flowchart and control rules are shown in Fig. 5(b). Chopping counter counts the chopping number n_c during one electric period. The comparator compares n_c with $Down_c$ or Up_c ($Down_c < Up_c$. $Down_c$ is used for acceleration process. $Down_c$ and Up_c are used for deceleration process).

During the acceleration process, if $n_c > Down_c$, the selector sets the selection signal s_g to a high level. The CCC controller will increase the reference current i_{ref} to change the speed n. The fuzzy angle regulator is not used, and θ_{on} and θ_{off} remain unchanged. n_c decreases with the increase in speed. When $n_c < Down_c$, the switching angles should be moved forward. If $\theta_{on} > -8°$, the selector assigns s_g to a low level, the fuzzy angle regulator will regulate θ_{on} and θ_{off}, and the CCC controller is not used. After θ_{on} and θ_{off} are moved forward, n_c will increase and be greater than $Down_c$, and the CCC controller is re-employed. During the acceleration process, the CCC controller and fuzzy angle regulator adjust the motor speed or torque in turn until θ_{on} and θ_{off} are set to $-8°$ and $10°$, respectively.

During the deceleration process, if $n_c < Down_c$, s_g is set to a low level. The fuzzy angle regulator regulates θ_{on} and θ_{off} to decrease speed. The CCC controller is not adopted, and i_{ref} remains unchanged. As the speed decreases when $Down_c < n_c < Up_c$, s_g is set to a high level. The CCC controller decreases i_{ref}, which further increases n_c. When $n_c > Up_c$ and $\theta_{on} < 0°$, the selector sets s_g to a low level, and the switching angles should be shifted backward to prevent the conduction angle from being turned on too early. The fuzzy angle regulator then moves θ_{on} and θ_{off} backward. Subsequently, n_c will be smaller than Up_c, and the CCC controller is re-employed. During the deceleration process, the CCC controller and

fuzzy angle regulator are used in turns to adjust the motor speed or torque until θ_{on} and θ_{off} are set to 0° and 18°, respectively. When $\theta_{on} = 0°$, the CCC controller will always be adopted to regulate the motor speed.

During the acceleration process, $Down_c$ is used for selecting the appropriate controller. During the deceleration process, $Down_c$ and Up_c are used for selecting the appropriate controller.

Given that the SRM drive is a nonlinear coupling system, fuzzy control algorithm is adopted to regulate the switching angles. The fixed dwell angle control is adopted, and θ_{on} and θ_{off} are controlled by the same fuzzy angle regulator. Fig. 5(c) shows the structural diagram of the fuzzy angle regulator. The error e and change of error Δe are used as the input variables, which are defined as

$$e(k) = T_{ref}(k) - T_e(k), \tag{12}$$

$$\Delta e(k) = e(k) - e(k-1) = T_e(k-1) - T_e(k), \tag{13}$$

$$T_{ref}(k) = T_{ref}(k-1), \tag{14}$$

where T_{ref} and T_e are the reference torque command and the motor output torque, respectively. Indices k and $k-1$ are the current and previous states of the motor, respectively.

$$e_N = G_e e, \tag{15}$$

$$\Delta e_N = G_{\Delta e} \Delta e, \tag{16}$$

$$\Delta \theta = G_{\Delta\theta} \Delta\theta_N, \tag{17}$$

where G_e, $G_{\Delta e}$, and $G_{\Delta\theta}$ are the input scaling and output scaling factors.

$$\theta_{on}(k) = \theta_{on}(k-1) + \Delta\theta(k) \tag{18}$$

$$\theta_{off}(k) = \theta_{off}(k) + \Delta\theta(k) \tag{19}$$

The rule forms used for the fuzzy angle regulator can be expressed as follows:

if $\quad \tilde{E} = \tilde{E}_i \quad$ and $\quad \tilde{\Delta E} = \tilde{\Delta E}_j$,

then $\quad \tilde{\Delta\theta} = \tilde{\Delta\theta}_{ij}$

$\quad i = 1, 2, ..., m, \quad\quad j = 1, 2, ..., n, \tag{20}$

where $\tilde{E}$ is the fuzzy set of the deviation of the motor torque, $\tilde{\Delta E}$ is the fuzzy set of the variation from the deviation of the motor torque, and $\tilde{\Delta\theta}$ is the fuzzy set of the increment of θ_{on} and θ_{off}.

V. SIMULATION ANALYSES

Fig. 6 shows the simulation waveforms at the startup stage of EV with $\gamma(k) = 0.5$ and $\gamma(k) = 1$. Figs. 6(a) and 6(c) illustrate the reference current i_{ref}, actual phase current i, and speed n. The chopping number n_c is greater than $Down_c$; thus, θ_{on} and θ_{off} are not changed, and CCC controller is adopted in the constant torque area. The time accelerating SRM from 0 r/min to 1200 r/min with $\gamma(k) = 1$ is only about half of that with $\gamma(k) = 0.5$. i tracks i_{ref} well by the hysteresis current
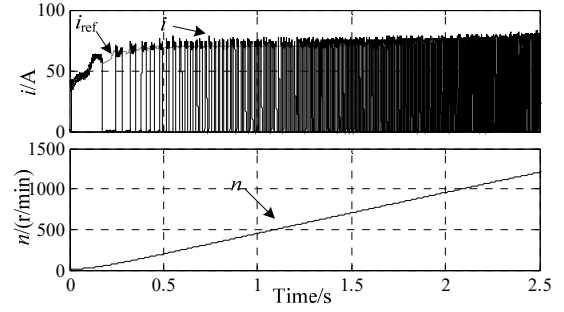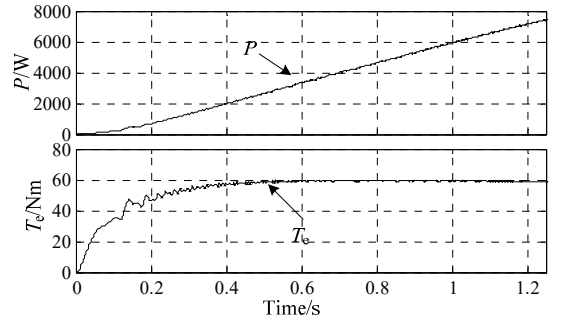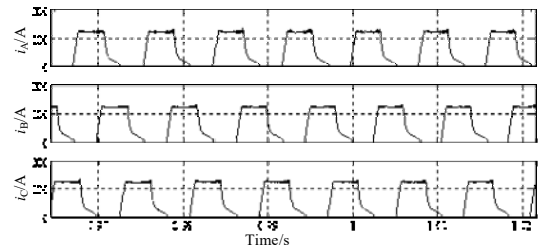

(a) i and n with $\gamma(k) = 0.5$.
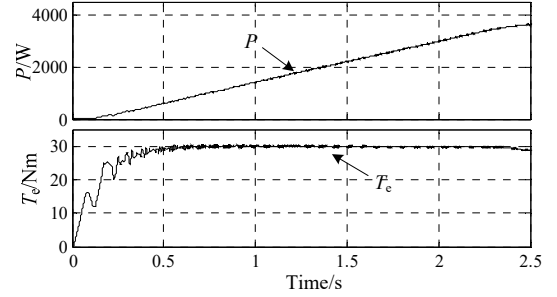
(b) P and T_e with $\gamma(k) = 0.5$.
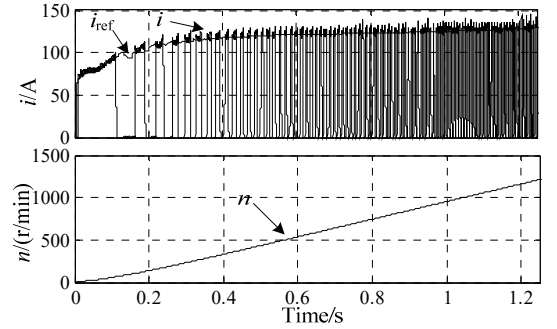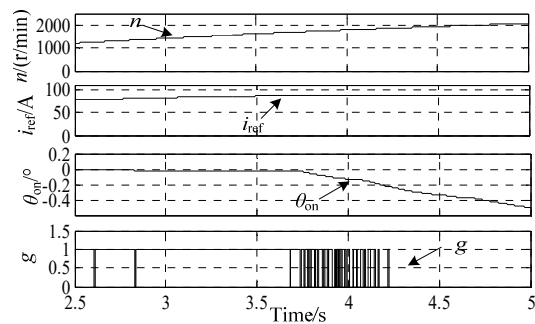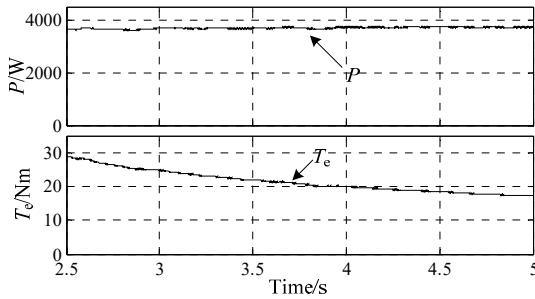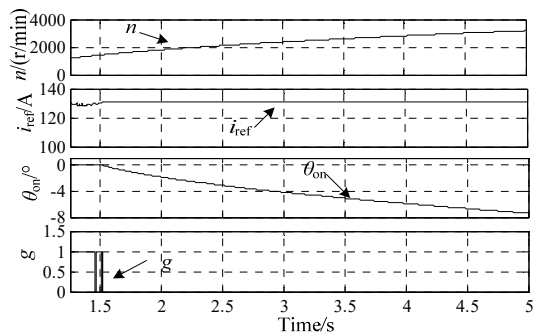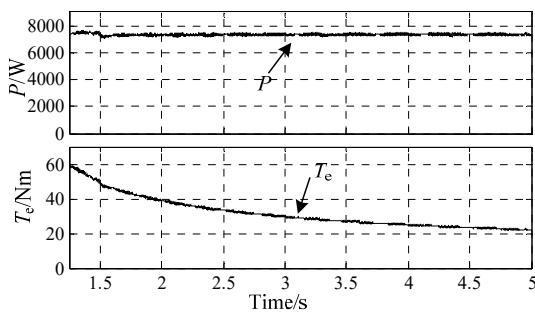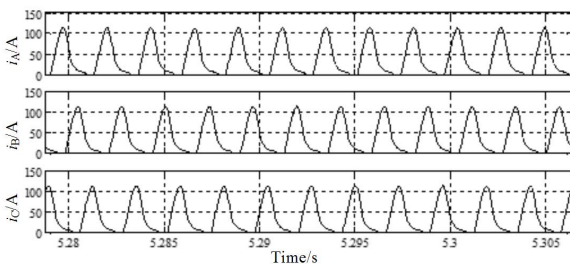

(c) i and n with $\gamma(k) = 1$.

(d) P and T_e with $\gamma(k) = 1$.

(e) Enlarged view of the three-phase currents.

Fig. 6. Simulation in the constant torque area.

(a) n, i_{ref}, θ_{on}, and s_g with $\gamma(k) = 0.5$.

(b) P and T_e with $\gamma(k) = 0.5$.

(c) n, i_{ref}, θ_{on}, and s_g with $\gamma(k) = 1$.

(d) P and T_e with $\gamma(k) = 1$.

(e) Enlarged view of the three-phase currents.

Fig. 7. Simulation in the constant power area.

controller. Figs. 6(b) and 6(d) illustrate the motor output power P and electromagnetic torque T_e with $\gamma(k) = 0.5$ and $\gamma(k) = 1$. At the startup stage, T_e rapidly increases to 30 Nm and 60 Nm with $\gamma(k) = 0.5$ and $\gamma(k) = 1$, respectively, and then remains unchanged in the constant torque area. P increases continuously and reaches 3250 W and 7500 W with $\gamma(k) = 0.5$ and $\gamma(k) = 1$, respectively. Fig. 6 (e) shows the enlarged view of the three-phase currents in the constant torque area.

Fig. 7 illustrates the simulation waveforms in the constant power area with $\gamma(k) = 0.5$ and $\gamma(k) = 1$. Figs. 7(a) and 7(c) illustrate the speed n, reference current i_{ref}, θ_{on}, and the selection signal s_g. If $n_c > Down_c$, $s_g = 1$; otherwise $s_g = 0$. When s_g is high, CCC is adopted and i_{ref} increases with n. When s_g is low, θ_{on} and θ_{off} are adjusted by the fuzzy control algorithm. s_g changes between 1 and 0, which indicates that the CCC controller and fuzzy angle regulator are adopted in turns. Figs. 7(b) and 7(c) show that T_e decreases gradually with the increase of n, and the output power P remains stable around 3250 W and 7500 W with $\gamma(k) = 0.5$ and $\gamma(k) = 1$, respectively. Fig. 7(e) shows the enlarged view of the three-phase currents in the constant power area.

VI. EXPERIMENTAL RESULTS

Fig. 8(a) shows the pictures of the test EV equipped with the designed SRM. The EV is a front-wheel drive, and the SRM drives the front wheels through gear reducer and differential. The parameters of the EV are listed in Table II. The small EV is operated on the flat ground. The weight of the small EV is 860 kg, including the driver. Fig. 8(b) shows the picture of the EV control system. MCU dsPIC30f6010A and CPLD EPM570T are used as the main and auxiliary controllers, respectively. The asymmetrical half-bridge power inverter is used for power conversion, and M57962AL is used as the driver chip.

Fig. 9 illustrates the experimental waveforms in the constant torque area. CH1 is the phase current waveform, and CH3 is the motor speed waveform in Fig. 9(a). The motor speed reaches 1200 r/min in approximately 1.2 s, which is the same as the simulation result shown in Fig. 6(c). In Fig. 9(b), CH1, CH2, and CH3 denote the three-phase current waveforms. CH4 represents the reference current i_{ref}. θ_{on} and θ_{off} of the SRM are set to 0° and 18°, and the sampling frequency and hysteresis bandwidth are 20 kHz and 8 A, respectively. The three-phase currents are limited within the hysteresis bandwidth and track the i_{ref} well using the digital hysteresis current controller.

Fig. 10 shows the experimental waveforms in the constant power area. CH1 is the speed n, CH2 is the reference current i_{ref}, CH3 is θ_{on}, and CH4 is the selection signal s_g in Figs. 10(a) and 10(b). During the acceleration process, CH1 and CH2 indicates that i_{ref} increases with n (Fig. 10(a)). θ_{on} and θ_{off} are unchanged in the initial stage, and n_c decreases. When $n_c <$
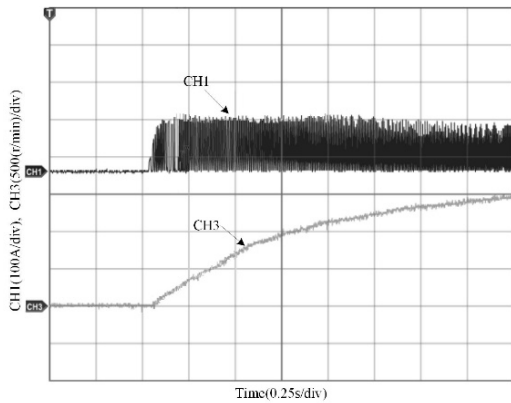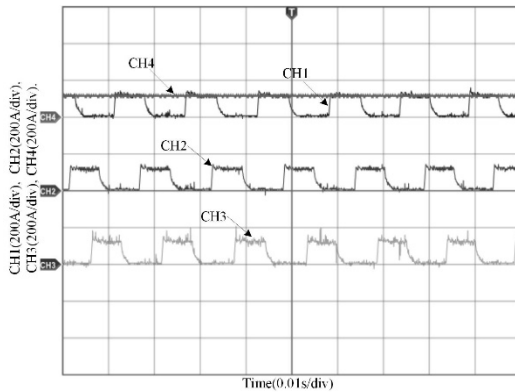
(a) EV.

(b) Control system.

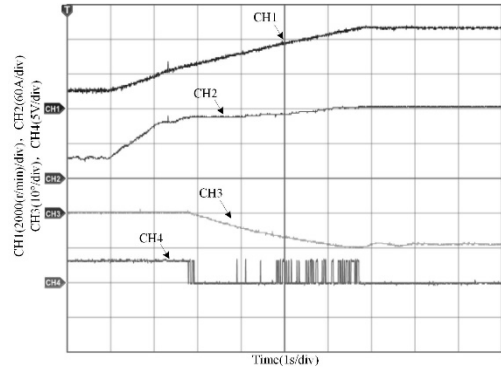Fig. 8. Pictures of the EV and controller.
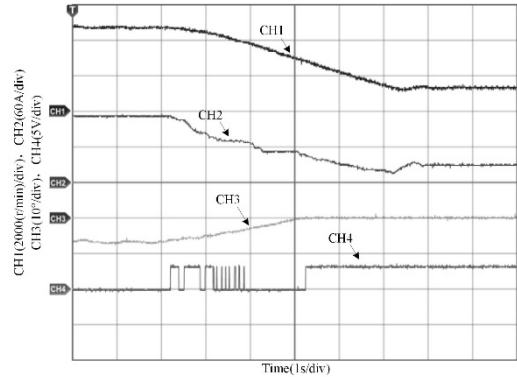

(a) Current and speed.

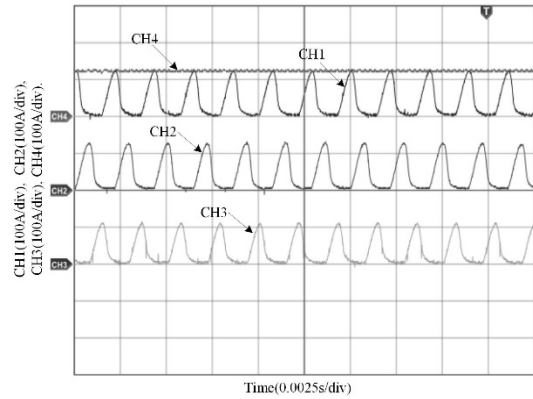(b) i_{ref} and phase current.

Fig. 9. Experiment in the constant torque area.

(a) Acceleration process.

(b) Deceleration process.

(c) i_{ref} and phase current.

Fig. 10. Experiment in the constant power area.

Down$_c$, θ_{on} is moved forward by the fuzzy angle regulator, as shown in CH3, and n_c increases. When $n_c >$ Down$_c$, the CCC controller regulates i_{ref}, as shown in CH2. CH4 indicates that s_g changes between 1 and 0; thus, the CCC controller and fuzzy angle regulator are employed in turns to regulate i_{ref} and the switching angles.

During the initial stage of deceleration process, given $n_c <$ Down$_c$, θ_{on} is moved backward by the fuzzy angle regulator, as shown in CH3 (Fig. 10(b)). i_{ref} is unchanged, as shown in CH2, and n_c increases. When Down$_c < n_c <$ Up$_c$, the CCC controller is adopted to decrease i_{ref}, and n_c further increases. When $n_c >$ Up$_c$, the fuzzy angle regulator moves θ_{on} and θ_{off} backward. CH4 indicates that s_g changes between 1 and 0;
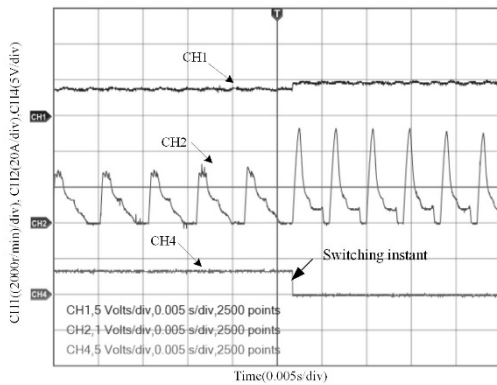
(a) Conventional control method with improper switching angles.
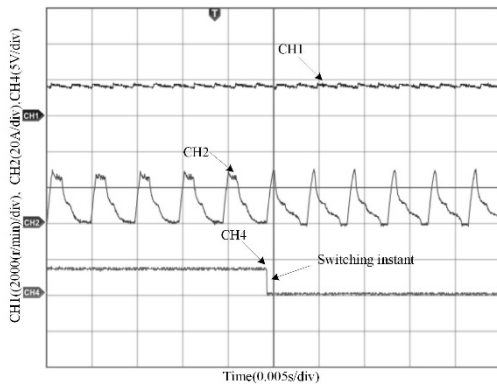
(b) Conventional control method with proper switching angles.
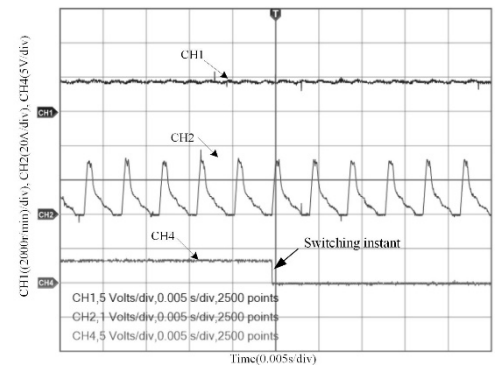
(c) Proposed control method.

Fig. 11. Comparison between the conventional control method and the proposed control method.

thus, the CCC controller and fuzzy angle regulator are employed in turns. When $\theta_{on} = 0°$, the CCC controller will always be used, as shown in CH4. Thus, θ_{on} and θ_{off} are adjusted by the proposed adaptive angle controller. In Fig. 10(c), CH1, CH2, and CH3 show the enlarged views of the three-phase current waveforms in the constant power area, and CH4 shows i_{ref}.

Fig. 11 shows the comparison between the conventional and the proposed control methods. CH1, CH2, and CH3 denotes the speed n, phase current i, and selection signal s, respectively. Fig. 11(a) shows that the phase current changes suddenly at the instance of CCC switching to APC if the turn-on and turn-off angles are improper, and the EV gives a sudden shake because of the motor torque variation. However,

the abrupt speed change cannot occur because of the system inertia moment when the EV runs on the ground. The driving wheels of the EV are lifted to eliminate the effect of the system inertia moment and reflect the evident change in motor speed using the conventional control method, as shown in Fig. 11(a). As shown in Fig. 11(b), the switching angles are selected appropriately by trial and error, and the speed will be smooth at the instance of CCC switching to APC. However, for EV applications, the loads are changed randomly according to traffic conditions. Thus, determining the proper turn-on and turn-off angles for all the loads is extremely difficult. The proposed method can adaptively regulate the switching angles at the instance of switching between the two modes, as shown in Fig. 11(c). The speed adjustment process of the EV is smooth, and the seamless transition between the two control modes is implemented. Thus, the method is remarkably suitable for EV applications.

VII. CONCLUSIONS

An EV model is developed in this study by combining the dynamic simulation model of SRM with the vehicle dynamic equations. The command torque of the motor drive system is given based on the accelerator pedal coefficient and motor operation areas. The AVAC control strategy is presented to improve the smoothness and comfort for EV applications, thereby avoiding the switching chattering between CCC and APC in the SRM drive. The flowchart and control rules of the control technique are also proposed. The main idea is to regulate θ_{on} and θ_{off} adaptively by the fuzzy angle regulator according to the chopping number during one electrical period. The CCC controller and fuzzy angle regulator are adopted in turns by comparing n_c with two constants, $Down_c$ or Up_c, during the speed regulation process. The proposed method does not need to determine θ_{on} and θ_{off} at the instances of switching between the two modes when the loads are usually changed. Thus, the proposed method is remarkably suitable for EV applications. An EV prototype is developed to experimentally verify the feasibility and effectiveness of the proposed control strategies.

REFERENCES

[1] M. Ehsani, Y. Gao, and A. Emadi, *Modern Electric, Hybrid Electric and Fuel Cell Vehicles Fundamentals, Theory, and Design*, CRC Press, New York, 2010.

[2] K. M. Rahman, B. Fahimi, G. Suresh, A. V. Rajarathnam, and M. Ehsani, "Advantages of switched reluctance motor applications to EV and HEV: design and control issues," *IEEE Trans. Ind. Appl.*, Vol. 36, No. 1, pp. 111-121, Jan./Feb. 2000.

[3] H. Chen and J. J. Gu, "Implementation of the three-phase switched reluctance machine system for motors and generators," *IEEE/ASME Trans. Mech.*, Vol. 15, No. 3, pp. 421–432, Jun. 2010.

[4] M. Dowlatshahi, S .M. Saghaiannejad, J. W. Ahn, and M. Moallem, "Copper loss and torque ripple minimization in switched reluctance motors considering nonlinear and magnetic saturation effects," *Journal of Power Electronics*, Vol. 14, No. 2, pp. 351-361, Mar. 2014.

[5] R. Madhavan and B. G. Fernandes, "Axial flux segmented SRM with a higher number of rotor segments for electric vehicles," *IEEE Trans. Energy Convers.*, Vol. 28, No. 1, pp. 203-213, Mar. 2013.

[6] H. Makino, T. Kosaka, and N. Matsui, "Digital PWM-control-based active vibration cancellation for switched reluctance motors," *IEEE Trans. Ind. Appl.*, Vol. 51, No. 6, pp. 4521-4530, Nov./Dec. 2015.

[7] A. Chiba, K. Kiyota, N. Hoshi, M. Takemoto, and S. Ogasawara, "Development of a rare-earth-free SR motor with high torque density for hybrid vehicles," *IEEE Trans. Energy Convers.*, Vol. 30, No. 1, pp. 175-182, Mar. 2015.

[8] K. Kiyota, H. Sugimoto, and A. Chiba, "Comparing electric motors: An analysis using four standard driving schedules," *IEEE Ind. Appl. Mag.*, Vol. 20, No. 4, pp. 12-20, Apr. 2014.

[9] B. Bilgin, A. Emadi, and M. Krishnamurthy, "Comprehensive evaluation of the dynamic performance of a 6/10 SRM for traction application in PHEVs," *IEEE Trans. Ind. Electron.*, Vol. 60, No. 7, pp. 2564-2575, 2013.

[10] V. Rallabandi and B. G. Fernandes, "Design procedure of segmented rotor switched reluctance motor for direct drive applications," *IET Electr. Power Appl.*, Vol. 8, No. 3, pp. 77-88, Mar. 2014.

[11] H. Cheng, H. Chen, and Z. Yang, "Design indicators and structure optimization of switched reluctance machine for electric vehicles," *IET Electr. Power Appl.*, Vol. 9, No. 4, pp .319-331, Apr. 2015.

[12] F. Yi and W. Cai, "Modeling, control, and seamless transition of the bidirectional battery-driven switched reluctance motor/generator drive based on integrated multiport power converter for electric vehicle applications," *IEEE Trans. Power Electron.*, Vol. 31, No. 10, pp. 7099-7111, Oct. 2016.

[13] X. Li and P. Shamsi, "Model predictive current control of switched reluctance motors with inductance auto-calibration," *IEEE Trans. Ind. Electron*, Vol. 63, No. 6, pp. 3934-3941, Jun. 2016.

[14] C. Gan, J. H. Wu, S. Y. Yang, and Y. H. Hu, "Phase current reconstruction of switched reluctance motors from DC-Link current under double high-frequency pulses injection," *IEEE Trans. Ind. Electron.*, Vol. 62, No. 5, pp. 3265-3275, May 2015.

[15] J. Ye, B. Bilgin and A. Emadi, "An offline torque sharing function for torque ripple reduction in switched reluctance motor drives," *IEEE Trans. Energy Convers.*, Vol. 30, No. 2, pp. 726-735, Jun. 2015.

[16] H. Zeng, H. Chen, and J. T. Shi, "Direct instantaneous torque control with wide operating range for switched reluctance motors," *IET Electr. Power Appl.*, Vol. 9, No. 9, pp. 578-585, Nov. 2015.

[17] H. Cheng, H. Chen, Q. L. Wang, S. H. Xu, and S. Y. Yang, "Design and control of switched reluctance motor drive for electric vehicles," *14th International Conference on Control, Automation, Robotics and Vision (ICARCV)*, pp. 1-6, 2016.

[18] H. Cheng, H. Chen, and Z. Yang, "Average torque control of switched reluctance machine drives for electric vehicles," *IET Electr. Power Appl.*, Vol. 9, No. 7, pp. 459-468, Aug. 2015.

[19] H. Hannoun, M. Hilairet, and C. Marchand, 'High performance current control of a switched reluctance machine based on a gain-scheduling PI controller," *Contr. Eng. Practice*, Vol. 19, No. 11, pp. 1377-1386, Aug. 2011.

[20] X. Li and P. Shamsi, "Inductance surface learning for model predictive current control of switched reluctance motors," *IEEE Trans. Transport. Electrific.*, Vol. 1, No. 3, pp. 287-297, Oct. 2015.

[21] J. Ye, P. Malysz, and A. Emadi, "A fixed-switching-frequency integral sliding mode current controller for switched reluctance motor drives," *IEEE J. Emerg. Sel. Topics Power Electron.*, Vol. 3, No. 2, pp. 381-394, Jun. 2015.

[22] H. Cheng, H. Chen, Z. Yang, and W. L. Huang, "Braking torque closed-loop control of switched reluctance machines for electric vehicles," *Journal of Power Electronics*, Vol. 15, No. 2, pp. 469-478, Mar. 2015.

He Cheng received his B.S. and Ph.D. degrees from the School of Information and Electrical Engineering, China University of Mining and Technology, Xuzhou, China in 2010 and 2015, respectively. He is a lecturer at the School of Electrical and Power Engineering, China University of Mining and Technology, Xuzhou, China. His current research interests include motor control, electric vehicles, and wind power generator control.

Hao Chen (SM'08) received his B.S. and Ph.D. degrees from the Department of Automatic Control, Nanjing University of Aeronautics and Astronautics, Nanjing, China in 1991 and 1996, respectively. In 1998, he became an associate professor at the School of Information and Electrical Engineering, China University of Mining and Technology, Xuzhou, China, where he has been a professor since 2001. From 2002 to 2003, he was a visiting professor at Kyungsung University, Busan, Korea. He has also been an adjunct professor at the University of Western Australia, Perth, Australia since 2008. He has authored one book and more than 170 papers. He has obtained 17 Chinese invention patents and 6 Chinese utility model patents. His current research interests include motor control, linear launcher, electric vehicles, electric traction, servo drives, and wind power generator control. Prof. Chen won the Prize of Science and Technology of Chinese Youth and the Prize of the Fok Ying Tong Education Foundation for Youth Teachers in 2004. He was awarded second prize in the Science and Technology advanced of Province and Ministry 6 times and third prize in the Science and Technology advanced of Province and Ministry 13 times. He was a candidate in the Chinese New Century Hundred, Thousand, and Ten Thousand Talents Engineering National Talent in 2007. He has also been awarded the government special allowance of the People's Republic of China State Department since 2006.

Shaohui Xu received his B.S. degree from the School of Information and Electrical Engineering, China University of Mining and Technology, Xuzhou, China in 2015. He is currently working toward his M.S. degree in the School of Electrical and Power Engineering, China University of Mining and Technology, Xuzhou, China.

Shunyao Yang received his B.S. degree from the School of Electrical Engineering, Nantong University, Nantong, China in 2015. He is currently working toward his M.S. degree in the School of Electrical and Power Engineering, China University of Mining and Technology, Xuzhou, China.